


Mechanisms of adsorbing hydrogen gas on metal decorated graphene

Yasmine S. Al-Hamdani 


*Department of Earth Sciences, University College London, London WC1E 6BT, United Kingdom;
Thomas Young Centre, University College London, London WC1E 6BT, United Kingdom;
and London Centre for Nanotechnology, University College London, London WC1E 6BT, United Kingdom*

Andrea Zen 

Dipartimento di Fisica Ettore Pancini, Università di Napoli Federico II, Monte Sant'Angelo, I-80126 Napoli, Italy

Angelos Michaelides 

Yusuf Hamied Department of Chemistry, University of Cambridge, Cambridge CB2 1EW, United Kingdom

Dario Alfè 

*Department of Earth Sciences, University College London, London WC1E 6BT, United Kingdom;
Dipartimento di Fisica Ettore Pancini, Università di Napoli Federico II, Monte Sant'Angelo, I-80126 Napoli, Italy;
Thomas Young Centre, University College London, London WC1E 6BT, United Kingdom;
and London Centre for Nanotechnology, University College London, London WC1E 6BT, United Kingdom*



(Received 3 August 2022; accepted 24 January 2023; published 13 March 2023)

Hydrogen is a key player in global strategies to reduce greenhouse gas emissions. In order to make hydrogen a widely used fuel, we require more efficient methods of storing it than the current standard of pressurized cylinders. An alternative method is to adsorb H_2 in a material and avoid the use of high pressures. Among many potential materials, layered materials such as graphene present a practical advantage as they are lightweight. However, graphene and other 2D materials typically bind H_2 too weakly to store it at the typical operating conditions of a hydrogen fuel cell, meaning that high pressure would still be required. Modifying the material, for example by decorating graphene with adatoms, can strengthen the adsorption energy of H_2 molecules, but the underlying mechanisms are still not well understood. In this work, we systematically screen alkali and alkaline-earth metal decorated graphene sheets for the static thermodynamic adsorption of hydrogen gas from first principles and focus on the mechanisms of binding. We show that there are three mechanisms of adsorption on metal decorated graphene and each leads to distinctly different hydrogen adsorption structures. The three mechanisms can be described as weak van der Waals physisorption, metal adatom facilitated polarization, and Kubas adsorption. Among these mechanisms, we find that Kubas adsorption is easily perturbed by an external electric field, providing a way to tune H_2 adsorption. This work is foundational and builds our understanding of H_2 adsorption under idealized conditions.

DOI: [10.1103/PhysRevMaterials.7.035402](https://doi.org/10.1103/PhysRevMaterials.7.035402)

I. INTRODUCTION

There is an urgent need to reduce the use of fossil fuels and develop alternative, less polluting methods of energy production. To this end, H_2 is long-standing potential candidate fuel [1]. There is an energy cost to producing H_2 in the first place, but H_2 molecules provide almost three times the energy density by weight as fossil fuels [2] and burning H_2 produces water with no additional harmful pollutants. In addition to burning, hydrogen can be combined with oxygen more efficiently in fuel cells, producing electricity and still only water as waste. At present, H_2 is stored as pressurized gas and more efficient H_2 storage materials are needed to propel this fuel into wide-scale use.

A promising method of storing hydrogen fuel is to physisorb H_2 molecules in a lightweight material. Cycling weakly adsorbed hydrogen gas through a material is expected to have minimal degradation effect on the storage material as

H_2 molecules remain intact. Other adsorption mechanisms of storage, such as the spillover method, rely on H_2 dissociating and forming covalent bonds with the storage material which makes the material more susceptible to deformation. In addition, weakly adsorbed hydrogen molecules require less energy to be released from a material relative to chemisorbed hydrogen atoms. The window for ideal H_2 adsorption energy can be estimated in a heuristic approach and considering the typical working temperature and pressure of fuel cells. The pressure (p), temperature (T), and the adsorption energy (E_{ads}), can be approximately related according to

$$p = e^{\frac{E_{\text{ads}}}{k_B T}} \frac{(2\pi m_{H_2})^{\frac{3}{2}}}{h^3} (k_B T)^{\frac{5}{2}} 2 \sinh\left(\frac{\hbar\omega_z}{2k_B T}\right), \quad (1)$$

where (k_B) is the Boltzmann constant, h is Planck's constant, m_{H_2} is the mass of H_2 , and ω_z is the harmonic frequency of vibration of the H_2 molecule with respect to the substrate. For

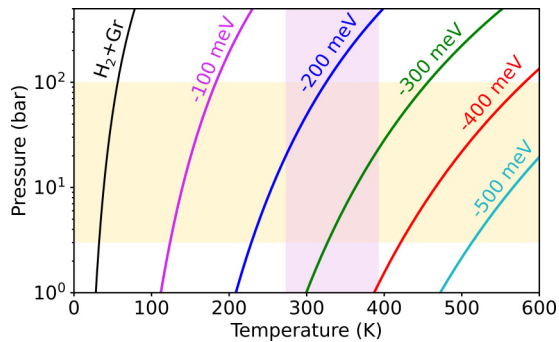


FIG. 1. The temperature-pressure profile of H_2 on pristine graphene at different adsorption energies indicated by the colored lines. The black line corresponds to the reference H_2 adsorption energy (-24 ± 11 meV) on pristine graphene from diffusion Monte Carlo [6]. An ideal range of H_2 vapor pressures for a typical fuel cell is indicated by the horizontal yellow region and the ideal working temperatures are indicated by the vertical pink region. The overlap in ideal temperature and pressure is roughly bounded by H_2 adsorption energies of -200 and -400 meV. See Eq. (1) for the relation between pressure, temperature, and adsorption energy.

a full account of how Eq. (1) is used and the approximations we make, see the Appendix. Polymer electrolyte membrane (PEM) fuel cells have been developed for a range of operating temperatures, with high-temperature PEM fuel cells functioning above 370 K [3,4]. Taking into account intermediate and high-temperature PEM fuel cells, we consider working temperatures of 270–390 K in this work. The typical operating pressure of a PEM fuel cell is ~ 3 bars of H_2 pressure [3], which means that the storage material must have a higher H_2 vapor pressure to readily release H_2 to the fuel cell. In addition, an upper bound of 100 bars has been proposed for the H_2 vapor pressure to avoid similar technological challenges as containing a highly pressurized gas [5]. Under such conditions, the energy of H_2 adsorption in a material is -200 to -400 meV per H_2 molecule as can be seen from Fig. 1.

The challenge of finding a material that binds H_2 suitably is also exacerbated by additional factors such as the weight and volume of the storage material [1,2,7]. Evidently, lighter and low-volume materials are required for practical and energy efficient fuel storage for mobile applications. There are various promising materials for H_2 storage and among them, we are interested in layered materials, such as graphene, as they are lightweight and are able to adsorb molecular hydrogen. However, the adsorption energy of H_2 on pristine graphene is predicted to be less than -50 meV [6], which is too weak for viable hydrogen storage (see Fig. 1). Structural defects and decoration by adatoms is known to enhance the adsorption energy of molecules on graphene [8] and there are countless combinations that can be considered. However, it is experimentally challenging to produce well controlled and characterized graphene with defects or adatoms and therefore it is difficult to ascertain the H_2 storage capacity of such potentially useful materials.

To date, there have been indications that decorating graphene with alkali and alkaline-earth metal adatoms facilitates H_2 adsorption [9–16], potentially yielding adequate H_2 capacities by weight. However, experimental information is

scarce and computational efforts to understand H_2 adsorption on metal decorated graphene are difficult to unify. For example, in different studies H_2 adsorption energies have been predicted using different density functional approximations preventing us from drawing reliable trends. In addition, the structure of H_2 molecules adsorbed around different metal adatoms on graphene has not received systematic focus and stands to be better understood.

Among alkali and alkaline-earth metals, Ca decorated graphene is one of the most studied systems [9–11,14,15,17,18]. This is partly due to favorable H_2 adsorption energies being predicted on this material as well as the relatively low cohesive energy of Ca, which is expected to prevent agglomeration on graphene. Specifically, Ataca *et al.* suggested over a decade ago that Ca adatoms facilitate the adsorption of H_2 molecules via Kubas-type binding [15]. This mechanism involves stabilizing the $3d$ state of Ca relative to $4s$ and donating electron density from $3d$ into the H_2 $1\sigma^*$ state [19]. Since then, a number of wave function based methods have been used to understand the Ca^+-4H_2 cluster (without a graphene substrate) and deduce whether a Ca adatom is able to bind H_2 using the Kubas mechanism [13,17,20–24]. The general conclusion from these works is that Ca is unlikely to bind H_2 using a Kubas-type binding and, hence, cast doubt on the accuracy of density functional theory (DFT) approximations. However, graphene has been shown to affect adsorption, and importantly, some metal adatoms (including Ca) make the adatom-graphene system metallic. Therefore, it is not straightforward to infer the nature of interaction on graphene from predictions on gas phase clusters.

Alongside Ca, other alkali and alkaline-earth metals on graphene have been considered for H_2 adsorption [9–12,16]. In brief, previous works have focused on assessing the adsorption strength of H_2 on a given material and in some cases methods without dispersion were used to predict adsorption energies [10,16]. We seek to build a better understanding of the mechanisms underpinning H_2 adsorption on different alkali and alkaline-earth metal adatoms on graphene. In this work, we systematically compute H_2 adsorption on alkali and alkaline-earth metal decorated graphene and draw mechanistic insights. We outline our computational setup and methods in Sec. II. In Sec. III we report the results of screening 1 to 7 H_2 molecules per metal adatom on graphene. We refine and analyze the adsorption of H_2 for a subset of systems in Sec. IV. In doing so, we elucidate the mechanisms of adsorption and find that they can be summarized in three physically distinct categories. We briefly consider the effects of adatom diffusion, H_2 dissociation, and alternative substrates in Sec. V. In Sec. VI, we report the effect of applying an external electric field on the H_2 interaction with the substrate and find that it depends strongly on the binding mechanism. We conclude in Sec. VII with a brief discussion of the results.

II. METHODS

The initial screening of adsorption energies was performed with CP2K version 7.1 [25,26] and Goedecker-Teter-Hutter pseudopotentials [27,28] in combination with DZVP-MOLOPT-SR-GTH basis sets [29]. A maximum

plane-wave cutoff of 300 Ry was used across 5 grids, with a relative cutoff of 30 Ry. Our CP2K calculations were spin polarized and performed at Γ point only for a 5×5 unit cell of graphene. The geometries were optimized with the BFGS method until the maximum force was less than 5×10^{-4} Ha a_0^{-1} . All parameters of the CP2K geometry optimizations can be seen in the example input in the Supplemental Material (SM) [30]. The Perdew-Burke-Ernzerhof (PBE) exchange-correlation functional [31] was used in combination with Grimme's D3 dispersion method [32] with zero-type damping and three-body Axilrod-Teller-Muto terms included, to account for van der Waals interactions. It is known that the choice of exchange-correlation functional has a notable impact on the H_2 adsorption energy on graphene-type surfaces [6,9]. Particularly in the case of physisorption, long-range dispersion interactions are expected to play an important role and therefore it is necessary to use a dispersion method. However, in the absence of experimental reference adsorption energies for the systems we are considering, it is difficult to ascertain which dispersion method yields the most accurate results. In general, dispersion methods have been shown to predict consistent structures and relative energies [33–38]. Absolute adsorption energies, on the other hand, can vary considerably among different density approximations. Previously, we established diffusion Monte Carlo (DMC) reference adsorption energies for H_2 inside and outside a carbon nanotube (CNT) and found that add-on dispersion methods are more accurate than seamless density-dependent dispersion functionals for the adsorption of H_2 inside a carbon nanotube [6]. Add-on dispersion methods include the D3 [32], D4 [39], and many-body-dispersion (MBD) [40,41] methods. These partially account for beyond two-body dispersion interactions which can play an important role in graphene-like materials [42]. In our work, we combine results from two DFT packages and therefore, to be consistent, we use PBE+D3 as it is implemented in CP2K and VASP. Note that PBE+MBD and PBE+D3 both predict an H_2 adsorption energy of -53 meV on pristine graphene, while DMC yields -24 ± 11 meV [6].

Metal decorated graphene ($M@Gr$) was modeled using a 5×5 unit cell of graphene with unit cell parameters optimized using PBE+D3. A single metal atom (M) was placed at the hollow site and fully optimized for Li, Be, Na, Mg, K, Ca, Rb, Sr, Cs, and Ba. H_2 molecules were placed upright relative to graphene and surrounding the metal atom in every initial structure. An interlayer spacing of 20 Å is applied along the z axis between graphene sheets and dipole corrections [43,44] along the z direction also computed. Up to 7 H_2 molecules were fully optimized on each $M@Gr$ system, totaling 70 systems, with all atoms in the cell allowed to relax. We report the results of this screening in Sec. III.

For a better understanding of the binding mechanisms and to assess the quality of the initial screening, we performed fine-grained optimizations of the resulting geometries from the screening. We used VASP version 5.4.4 [45–48] with standard PAW potentials and a 500 eV plane-wave cutoff. Since the neutral metal atoms are easily ionized, potentials with explicit semicore s states were used for all metals. Na has the highest-energy core states among the metal atoms we considered and we found that the interaction energy of $4H_2$

on $Na@Gr$ is converged with a 500 eV plane-wave cutoff to within 2 meV. In addition, the decoration of graphene with metal atoms makes the system metallic and hence we used a dense \mathbf{k} -point mesh of $9 \times 9 \times 1$ centered on Γ . We found the interaction energy of $4H_2$ on $Ca@Gr$ is converged within 1 meV per H_2 using a \mathbf{k} -point mesh of $5 \times 5 \times 1$ and therefore we expect an even denser mesh to be sufficient for all the systems we considered. The fine-grained geometry relaxations for 3–5 H_2 molecules on each substrate were converged with residual forces less than 0.01 eV Å $^{-1}$. Densities of states were obtained using a $15 \times 15 \times 1$ \mathbf{k} -point mesh and the SUMO code [49] was used in postprocessing the data.

In Sec. V we report a diffusion barrier for Ca on graphene, H_2 dissociative adsorption, and a few H_2 binding energies on metal decorated bilayer graphene and metal decorated $Gr/Ni(111)$. The Ca diffusion barrier was computed using the climbing-image nudged elastic band (NEB) method with five replicas and a spring force constant of 5 eV Å $^{-2}$ with nudging [50–52]. For bilayer graphene, a 5×5 unit cell of AB -stacked double-layer graphene was modeled where the interlayer spacing between the two sheets of graphene is 3.501 Å along the z axis. The $Gr/Ni(111)$ slab contains a single layer of graphene on five layers of Ni atoms, with two of the bottom layers fixed at the experimental bulk lattice constant for Ni. The slab structure contains 125 Ni atoms and 50 C atoms. A \mathbf{k} -point mesh of $5 \times 5 \times 1$ was used in these systems. Further details on the setup and numerical settings of the computations for Sec. V can be found in the SM [30].

For the application of external electric force fields in Sec. VI, we used a sawtooth potential as implemented in VASP and applied the field along the z direction in the unit cell, i.e., perpendicular to the graphene sheet. We also performed geometry optimizations of $4H_2$ adsorbed on $Ca@Gr$ at two electric fields (0.2 V Å $^{-1}$ and -0.2 V Å $^{-1}$) using a \mathbf{k} -point mesh of $5 \times 5 \times 1$.

III. SCREENING H_2 ADSORPTION ON METAL DECORATED GRAPHENE

Decorating graphene with single metal atoms has previously been found to strengthen the adsorption of H_2 molecules for some metals such as Ca and Li [15,16]. In some cases, such as $Mg@Gr$, the adsorption of H_2 remains weak [12]. We focus specifically on alkali and alkaline-earth metals, from Li to Ba, with the aim to understand the mechanisms underpinning the interactions. The indication from previous works is that dispersion interactions contribute significantly to the adsorption energy [53] and H_2 is bound too weakly to be useful for hydrogen storage [8,54]. However, it appears from the range of adsorption energies reported that it is difficult to establish consistent adsorption energies from DFT approximations [54]. Moreover, a systematic analysis of the adsorption geometries is missing from our current understanding and we aim to address that here. An approximate overview of the relative strength of H_2 adsorption as the number of H_2 molecules is increased is given by the crude screening in this section. The results of the rapid DFT screening of H_2 adsorption energies on $M@Gr$, using CP2K and atom centered basis sets, is shown

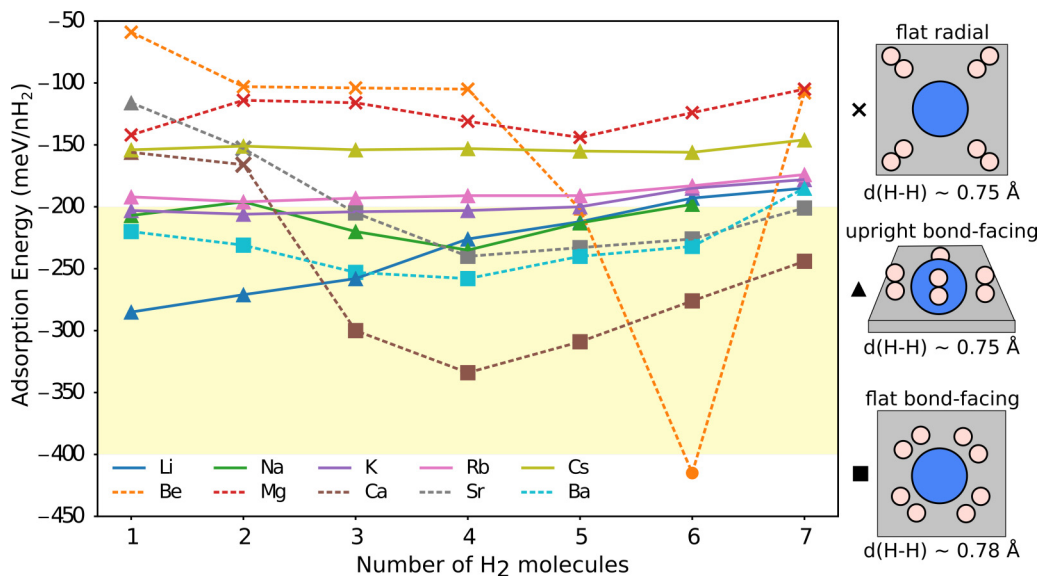


FIG. 2. Preliminary screening of H₂ adsorption on group 1 (solid lines) and group 2 (dashed lines) $M@Gr$. PBE+D3 adsorption energies shown here (in meV) are approximate only. For a converged PBE+D3 adsorption energies, see Table I, where a subset of systems is reported. The symbols indicate the optimized orientation of H₂ molecules around the metal atom. Triangles indicate upright bond-facing (BF), squares indicate flat BF, and crosses indicate flat radial configuration. The three mechanisms are also depicted on the right. The circle ($6H_2+Be@Gr$) indicates dissociative adsorption of H₂ has occurred. Average H-H bond lengths are also given for each mechanism of binding. The yellow shaded region from -200 to -400 meV indicates an estimated range of suitable adsorption energies for storage in operation with fuel cells.

in Fig. 2. The adsorption energy (E_{ads}) is defined as

$$E_{\text{ads}} = (E_{nH_2+M@Gr}^{\text{tot}} - E_{M@Gr}^{\text{tot}} - nE_{H_2}^{\text{tot}})/n, \quad (2)$$

where $E_{nH_2+M@Gr}^{\text{tot}}$ is the total energy of H₂ molecules adsorbed on $M@Gr$, $E_{M@Gr}^{\text{tot}}$ is the total energy of the fully relaxed $M@Gr$ substrate, $E_{H_2}^{\text{tot}}$ is the total energy of the gas phase relaxed H₂ molecule, and n is the number of H₂ molecules adsorbed.

Screening calculations were performed at the Γ point only and using atom-centered basis sets without correcting for basis set superposition error. As a result, the PBE+D3 ad-

sorption energies in Fig. 2 are likely to be overestimated. For reliable PBE+D3 adsorption energies, as obtained from VASP using a well-converged setup (discussed in Sec. IV), see Table I, where we report adsorption details for systems with 3–5 H₂ molecules, as well as the adsorption energy of metal adatoms on graphene.

The geometry optimization of H₂ molecules on $M@Gr$ broadly yields three orientations of H₂ molecules, as can be seen from Fig. 2. There are several features to note from these preliminary adsorption profiles. First, the weakest adsorption profile is seen for Be@Gr and Mg@Gr, where the H₂

TABLE I. Adsorption properties of 3–5 H₂ molecules adsorbed on alkali and alkaline-earth $M@Gr$ from PBE+D3. $E_{M@Gr}$ is the fully relaxed adsorption energy of the metal adatom (M) on a 5×5 unit cell of graphene (Gr) and d_{M-Gr} is the corresponding separation distance along the z axis considering the average position of all carbon atoms. $E_{\text{ads}}^{nH_2}$ is the average adsorption energy per H₂ molecule when nH_2 molecules are adsorbed (in eV). The H-H bond lengths, d_{H-H} , and average $M-H_2$ distances, d_{M-H_2} , are reported for the $4H_2+M@Gr$ system in Å. In the upper section, Li to Cs, the H₂ molecules are in an upright bond-facing. H₂ molecules are in flat radial configuration on Be@Gr and Mg@Gr. In the lower section of the table, Ca to Ba, H₂ molecules are in a flat bond-facing configuration. The values reported here correspond to spin-polarized geometry optimizations performed with $9 \times 9 \times 1$ k-point mesh and force convergence criterion of 0.01 eV \AA^{-1} .

| Adatom (M) | $E_{M@Gr}$ (eV) | d_{M-Gr} (Å) | $E_{\text{ads}}^{3H_2}$ (eV) | $E_{\text{ads}}^{4H_2}$ (eV) | $E_{\text{ads}}^{5H_2}$ (eV) | d_{H-H} (Å) | d_{M-H_2} (Å) |
|----------------|-----------------|----------------|------------------------------|------------------------------|------------------------------|---------------|-----------------|
| Li | -1.279 | 1.704 | -0.187 | -0.161 | -0.141 | 0.755 | 2.348 |
| Na | -0.719 | 2.189 | -0.176 | -0.173 | -0.156 | 0.756 | 2.516 |
| K | -1.200 | 2.571 | -0.137 | -0.137 | -0.121 | 0.754 | 2.964 |
| Rb | -1.262 | 2.730 | -0.128 | -0.128 | -0.112 | 0.754 | 3.209 |
| Cs | -1.466 | 2.903 | -0.117 | -0.118 | -0.102 | 0.753 | 3.435 |
| Be | -0.181 | 3.218 | | -0.088 | | 0.754 | 2.875 |
| Mg | -0.281 | 3.322 | | -0.068 | | 0.754 | 3.180 |
| Ca | -0.741 | 2.314 | -0.142 | -0.190 | -0.178 | 0.784 | 2.287 |
| Sr | -0.753 | 2.497 | -0.096 | -0.135 | -0.132 | 0.779 | 2.478 |
| Ba | -1.198 | 2.577 | -0.159 | -0.181 | -0.163 | 0.771 | 2.722 |

molecules prefer to be flat on the graphene sheet and pointing radially to the metal atom. An example of this flat radial configuration is illustrated in Fig. 2. This configuration suggests the main contribution to adsorption is between H_2 and graphene, with an additional weak interaction with the metal adatom. Note that Be has a degeneracy in its valence states that is known to make it reactive with hydrogen, forming Be-H bonds. This occurs in one of the geometry optimizations, when 6 H_2 molecules are placed near Be, leading to the dissociative adsorption of a H_2 molecule. Therefore, Mg and Be are not likely to be suitable adatoms on graphene for H_2 storage via weak adsorption. Second, all alkali $M@Gr$ substrates adsorb H_2 in the upright bond-facing (BF) configuration and the adsorption energy profile is near-linear with increasing number of molecules. For K, Rb, and Cs, the adsorption profile is particularly flat, varying by less than 30 meV in the adsorption energy per H_2 molecule, from 1 to 7 H_2 molecules. Adsorption is strongest among alkali metals for Li@Gr with up to 3 H_2 molecules. However the H_2 adsorption energy on Li@Gr shows a steady weakening with increasing number of H_2 molecules. This is due to H_2 molecules not fitting around the small Li adatom and therefore spreading farther away on the surface. In the case of Na@Gr, there is a small ~ 40 meV variation in the H_2 adsorption energy, with the most favorable binding occurring at 4 H_2 molecules. However, the configurations remain upright BF across the profile. We can see from Fig. 2 that another configuration of H_2 (flat BF) results on Ca, Sr, and Ba, decorated graphene. The flat BF configuration is not exclusive on these substrates and both upright BF and flat radial configurations can be seen for 1, 2, and 7 H_2 adsorbed molecules. Indeed, these heavier alkaline-earth elements exhibit the most variation in their H_2 adsorption profiles, varying by more than 70 meV with respect to the number of H_2 molecules adsorbed. However, the strongest adsorption for graphene decorated with Ca, Sr, and Ba is consistently predicted at 4 H_2 molecules in the flat BF orientation. In addition, the flat BF configurations of H_2 have a distinct H-H bond length of 0.78 Å, i.e., a 4% elongation with respect to the equilibrium bond length. On the other hand, in the flat radial and upright BF configurations the H-H bond length stays close to equilibrium (0.75 Å). The longer bond length for the flat BF configuration of H_2 is therefore indicative of a different interaction mechanism that involves the $1\sigma^*$ state of the H_2 molecule. This is known as the Kubas-type bonding interaction and it has been discussed in previous works that considered Ca adatoms [13,15,17,54]. Here, we see that this configuration manifests more generally when graphene is decorated with alkaline-earth metals that have available d states, such as Sr and Ba. We also describe this mechanism in more detail in Sec. IV.

Our screening of H_2 adsorption on alkali and alkaline-earth metal decorated graphene suggests that the strongest nondissociative adsorption of H_2 for more than 3 molecules per adatom occurs on Ca, Sr, and Ba decorated graphene. For fewer than 3 H_2 molecules per adatom, Li@Gr is predicted to bind H_2 strongly. However, adsorption energies in this screening are only approximate as loose technical parameters have been used and the PBE+D3 method is also a source of uncertainty. In the next section we report adsorption energies

from well-converged basis set, Brillouin sampling, and geometry optimizations for a subset of systems with PBE+D3.

IV. MECHANISM OF ADSORPTION AND THE ROLE OF GRAPHENE

To understand the electronic structure mechanisms underlying the three distinct configurations of H_2 adsorption that we find, we performed well-converged geometry relaxations on all adatom systems with 3–5 H_2 molecules from Sec. III. The computational details are given in Sec. II and we note that the main improvement is in the k -mesh density (using a $9 \times 9 \times 1$ grid on a 5×5 unit cell of graphene) and the use of a plane-wave basis set as implemented in VASP. We have also performed calculations with alternative starting geometries to see if flat BF configurations can be stabilized over upright BF on alkali metals, and vice versa on alkaline-earth metals. We find that the orientation of H_2 molecules predicted in Sec. III is consistent and that the graphene-adatom distances change by less than 5% or 0.16 Å. Similarly, the H_2 -adatom distance changes by, at most, 10% or 0.28 Å. A detailed report of the separation distances for each system from CP2K and VASP is provided in Table S1 of the SM [30].

The PBE+D3 H_2 adsorption energies on $M@Gr$ substrates and metal adatom adsorption energies on graphene are reported for well-converged optimized structures in Table I. The PBE+D3 metal adatom adsorption energies ($E_{M@Gr}$) show that Mg and Be adsorb weaker than -300 meV on graphene, while other metal adatoms adsorb by over -700 meV. The average H_2 -metal adatom and graphene-metal adatom separation distances are also reported in Table I for each metal considered. We can see that stronger H_2 adsorption is accompanied by shorter H_2 -metal adatom separation distances and that Ca and Ba adatoms best facilitate the adsorption of H_2 molecules with adsorption energies of up to -190 and -181 meV per H_2 molecule, respectively. It is evident that the screening in Sec. III led to overestimated adsorption energies, but we note that the most favorable adsorption energy predicted here with PBE+D3 is within 10 meV of the range that is expected to be useful for H_2 storage. It is important to note, however, that the accuracy of PBE+D3 is not established for predicting $M@Gr$ systems as there is no experimental or theoretical reference information; nonetheless we expect that the physical trends obtained from DFT are physically consistent.

First, we focus on the $4H_2+Ca@Gr$ system, where the adsorption energy is the strongest and there is a long-standing effort to establish whether the system is viable for H_2 storage. The unit cell, adsorption configuration, and charge density difference for adsorbing 4 H_2 molecules can be seen in Fig. 3. We can see that there is charge accumulation in the region between the Ca adatom and the H_2 molecules and charge depletion above the Ca adatom and within the H-H bonding regions, in agreement with the work of Ataca *et al.* [15]. Charge depletion along H_2 covalent bonds is consistent with longer H-H bond lengths, from 0.75 Å in the gas phase equilibrium structure to 0.78 Å in the adsorbed flat BF configurations. This form of binding has been discussed previously [15,54] and is known as a Kubas interaction. More specifically, it arises from stabilization of the $3d$ state of Ca over

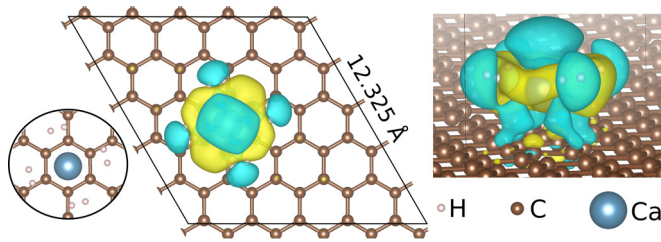


FIG. 3. The $4\text{H}_2+\text{Ca@Gr}$ system showing the geometry of H_2 molecules around Ca and the charge redistribution upon adsorbing H_2 molecules. The unit cell used is indicated in the middle panel. Charge density difference is shown between 4H_2 and Ca@Gr using an isosurface level of $0.002 e \text{ \AA}^{-3}$. Charge density depletion is shown in blue and charge density accumulation is shown in yellow.

the $4s$ state and back-donation of electron density from the valence Ca- d state to the $1\sigma^*$ state of the H_2 molecule. This mechanism is corroborated in the projected density of states (PDOS) of $4\text{H}_2+\text{Ca@Gr}$, shown in Fig. 4(c). In addition, a Bader charge analysis [50,55,56] of the system shows that Ca has a partial positive charge of $+1.3 e$ on the Ca atom, which is consistent with the partial depopulation of the Ca- $4s$ state. We also find that one H atom in each H_2 molecule has accumulated a small Bader partial charge of $-0.15 e$. H_2 bond weakening can also be found on Sr@Gr and Ba@Gr , indicating that the Kubas mechanism underpins the adsorption of H_2 in these systems also.

Adsorbed H_2 molecules on Li, Na, K, Rb, and Cs metal decorated graphene, which are in an upright BF configuration, do not exhibit H-H bond weakening and the effect on the charge density from adsorption is also distinctly different (see SM [30] for the charge density difference for 4H_2 on Na@Gr). Indeed, the PDOS of 4H_2 on K@Gr in Fig. 4(a) shows no K occupied states near the Fermi energy, indicating complete charge transfer of the K valence electron to graphene and no occupation of the $1\sigma^*$ states of the H_2 molecules. This is confirmed by a Bader analysis of the system, showing that K has a positive partial charge of $+0.9 e$ and H atoms have not gained (or lost) electron density. Given that alkali adatoms lose their single valence electron to graphene, the resulting positively charged adatom facilitates the adsorption of H_2 on the surface through a direct static polarization interaction with H_2 molecules. We can see from the adsorption energies in Table I that the order of H_2 adsorption strength coincides with the polarizing strength of the alkali cation for 3H_2 adsorbed, such that the Li adatom binds H_2 the most strongly and the Cs adatom binds H_2 the least among the alkali metal adatoms we consider. With more than three H_2 molecules adsorbed, the trend holds from Na as Li is small and H_2 molecules become sterically hindered.

When the adsorption of H_2 is very weak, as in the case of Be and Mg decorated graphene, H_2 is radially orientated to the adatom while lying flat on graphene. The resulting H_2 configuration is similar to H_2 physisorption on pristine graphene [6]. Indeed, it was previously reported that the PBE+D3 adsorption energy of H_2 on pristine graphene is -53 meV [6], while we find that the adsorption energy is -68 meV on Mg@Gr . The different adsorption mechanism of H_2 on Mg and Be adatoms to other alkaline-earth metals can be

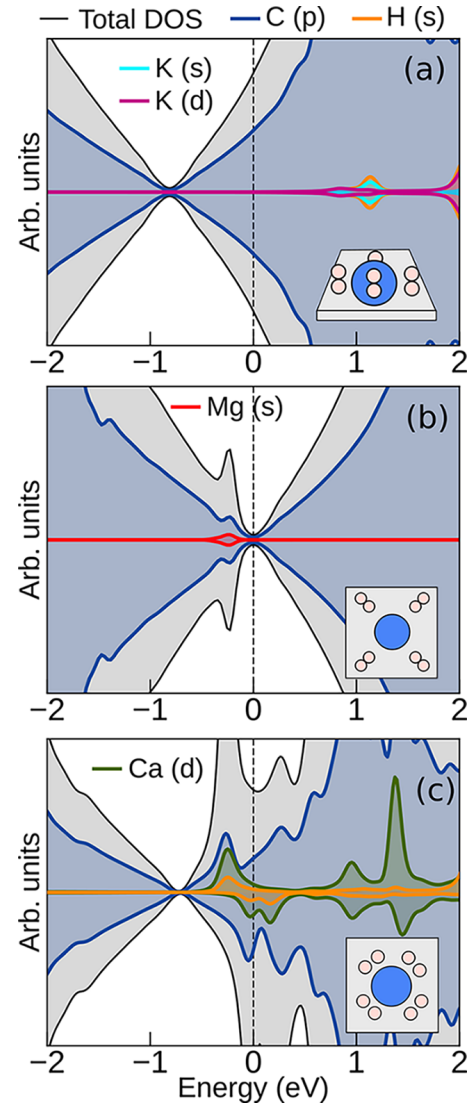


FIG. 4. The projected density of states (PDOS) within $\pm 2 \text{ eV}$ of the Fermi energy for 4H_2 adsorbed on (a) K@Gr , (b) Mg@Gr , and (c) Ca@Gr . The PDOS has been shifted to the Fermi energy for each system. The gray shaded region indicates the total DOS. H- s projection shown in orange and C- p projection shown in blue. H- s near the Fermi energy is due to the $1\sigma^*$ state of H_2 , while the 1σ state around -8 eV relative to the Fermi energy cannot be seen in this energy window. The projection is over spherical functions centered on the atoms and as such, the sum of projected states may not sum to the total DOS. A schematic of the configuration of 4H_2 for each $M@Gr$ system is shown in the insets.

understood in terms of the metal atom electronic structure. First, the valence $2s$ and $3s$ electrons of Be and Mg, respectively, cannot be stabilized to a d state and therefore they cannot bind H_2 molecules via Kubas bonding. Second, the ionization energies of Be and Mg are too high for graphene to oxidize the adatoms. Indeed, a Bader charge analysis of $4\text{H}_2+\text{Mg@Gr}$ shows that Mg has only a small positive partial charge of $+0.3 e$. The PDOS of $4\text{H}_2+\text{Mg@Gr}$ in Fig. 4(b) demonstrates the intact Mg valence state and can be seen as an occupied s state just under the Fermi energy of graphene. As a

result, Be and Mg remain uncharged atoms that H₂ molecules weakly interact with.

V. INSIGHTS FOR BRIDGING TOWARD EXPERIMENT

The binding mechanisms we outlined based on static thermodynamic models are foundational and several physical effects can be considered to bridge toward experiment. Here, we gauge the effect of a few important physical contributions that can play a role in H₂ binding—specifically, adatom diffusion, H₂ dissociation, and the experimental form of graphene. Details of the computational setups can be found in Sec. II and the SM [30]. First, we gauge the feasibility of Ca adatom diffusion across the graphene surface and the dissociative adsorption of H₂ on Ca@Gr as it is one of the most promising systems for H₂ binding according to our screening. We used the NEB method [51,52] to predict the energy barrier for a Ca adatom to diffuse from its most stable adsorption site on pristine graphene, to the next most stable adsorption site. We find that the PBE+D3 energy barrier for Ca diffusion on graphene is 0.14 eV which can be considered thermally accessible under ambient conditions. Previous works report similar energy barriers, 0.12–0.16 eV, for Ca diffusion on graphene [15,57,58]. Meanwhile, H₂ dissociating on Ca@Gr would indicate storage via the spillover effect instead and we gauge the likelihood of this by fully relaxing 2H+Ca@Gr, with H atoms chemisorbed on graphene in the vicinity of Ca for two configurations. The fully relaxed structures can be found in the SM [30]. We find that 2H+Ca@Gr is ~ 1.7 eV less stable than H₂+Ca@Gr, suggesting that intact H₂ is thermodynamically stable on Ca@Gr. These calculations provide preliminary indications, but further work is needed to cement our predictions. Second, in experiment, graphene can be found stacked in a few single layers, known as multilayer graphene, and is also typically supported by a substrate such as silicon dioxide or a metal surface. A great deal of work has focused on uncovering the effects of different metal substrates on the structural and electronic properties of graphene. Here, we briefly explore the role of AB-stacked bilayer graphene (GrGr) and near-fully commensurate metal substrate, Ni(111), on the H₂ binding mechanisms found in Sec. IV. We fully relax three different binding motifs with GrGr: 4H₂+Ca@GrGr, 4H₂+K@GrGr, and 4H₂+Mg@GrGr. The resulting binding configurations and the adsorption energies per H₂ molecule are in close agreement to those established on single-layer graphene in Sec. IV. The adsorption energy per H₂ molecule is only 2 meV weaker on GrGr for Mg and Ca adatoms, and 7 meV stronger with K as the adatom. Therefore, we expect the effect of multilayer graphene to be small for the binding mechanisms of H₂. Note that we only consider adatoms at the surface and not in the interlayer regions. Ni(111) is a widely used and commercially available metal substrate for graphene, which minimally strains graphene thanks to the commensurate structure of the surface. Interestingly, Gr/Ni(111) exhibits two binding minima according to first-principles predictions: a physisorption minimum (>3 Å) and a more thermodynamically favorable chemisorption minimum (~ 2 Å) [59] that is in line with experiment [60]. We briefly consider the impact of chemisorbed graphene on a Ni(111) substrate (GrNi) on the binding mechanisms in 4H₂+Ca@GrNi, 4H₂+K@GrNi,

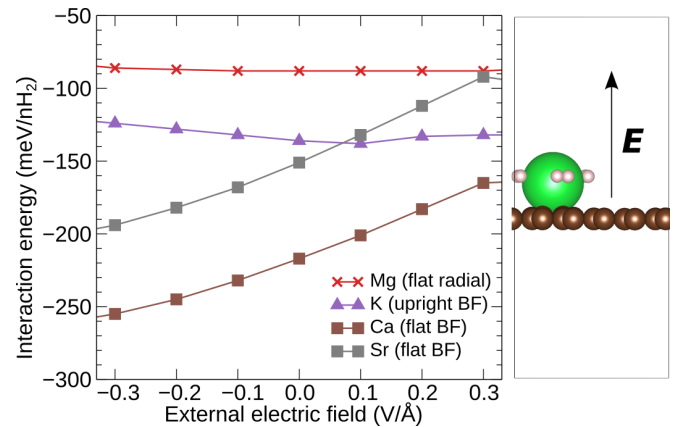


FIG. 5. Interaction energy per *unrelaxed* H₂ molecule in 4H₂+K@Gr (purple triangle), 4H₂+Ca@Gr (brown square), 4H₂+Sr@Gr (gray square), and 4H₂+Mg@Gr (red cross) with respect to the electric force field (in V Å⁻¹). The structures used in calculating the interaction energy are kept fixed at the zero-field adsorbed configuration for each metal element. The interaction energy therefore does not convey the atomically relaxed adsorption energy. The external field was applied in the direction perpendicular to the graphene sheet, as shown in the side panel, and defined in terms of a positive test charge.

and 4H₂+Mg@GrNi. We find that the adsorption structure and energy in 4H₂+K@GrNi is practically unaffected with respect to 4H₂+K@Gr. In 4H₂+Mg@GrNi, we find that H₂ and Mg remain weakly physisorbed and in the same orientation, while the adsorption energy per H₂ is strengthened by ~ 37 meV with respect to 4H₂+Mg@Gr. Most notably, we find that H₂ molecules relax into an upright bond-facing orientation in 4H₂+Ca@GrNi and the adsorption energy per H₂ molecule is also strengthened by ~ 38 meV with respect to 4H₂+Ca@Gr. Therefore, there is a promising indication that the metal substrate used to support graphene can have a significant impact on the binding of H₂ and can be an important feature to exploit in future works.

VI. TUNING THE H₂ ADSORPTION ENERGY USING AN ELECTRIC FIELD

An ideal storage material for H₂ would allow the reversible cycling of gas and easy tuning of the H₂ adsorption energy would be an additional welcome feature. To this end, we report the effect of applying an electric field on the interaction with H₂ bound via the three mechanisms we have established. For the results in Fig. 5 we do not allow the atomic positions to relax under the applied electric field and as such, the results indicate the response of only the electron density to an applied field (i.e., the high-frequency limit). Specifically, we look at the interaction defined as

$$E_{\text{int}} = (E_{\text{ads}}^{\text{ads}@0} - E_{M@Gr}^{\text{ads}@0} - E_{4H_2}^{\text{ads}@0})/4, \quad (3)$$

where $E_{\text{ads}}^{\text{ads}@0}$ is the total energy of the system with 4H₂ adsorbed on $M@Gr$ fully optimized at zero field, while $E_{M@Gr}^{\text{ads}@0}$ and $E_{4H_2}^{\text{tot}}$ are the total energies of unrelaxed $M@Gr$ and 4H₂ in the adsorption configuration at zero field. Since Eq. (3) does not take into account any atomic relaxation, the resulting in-

teraction energies do not convey the final adsorption energy at the applied electric field (low-frequency limit). For example, it can be seen from Fig. 5 that E_{int} at zero field is lower than E_{ads} reported in Table I and this is due to the unrelaxed reference subsystems in the definition of E_{int} .

It can be seen from Fig. 5 that the effect of an external electric field (applied in the z direction) on the H_2 interaction energy with K and Mg decorated graphene is minimal. The results suggests that interaction with H_2 is not easily perturbed for H_2 bound using weak physisorption (flat radial configurations on Be@Gr and Mg@Gr) or static polarization interactions (upright BF on alkali@Gr systems). However, it can be seen from Fig. 5 that the H_2 molecule interaction with Ca and Sr decorated graphene is strongly affected by an external electric field. With electric fields from -0.3 V \AA^{-1} to 0.3 V \AA^{-1} in the z direction, the interaction is decreased by $\sim 100 \text{ meV}$ per H_2 molecule. Since a positive electric field perpendicular to the graphene sheet draws electrons from the adatom toward graphene, H_2 adsorption weakens as the adatom electron density is depleted.

On relaxation of the $4\text{H}_2+\text{Ca@Gr}$ system under a positive electric field, we find that the H_2 molecules reorient themselves to the upright BF configuration (see Fig. 6) while the H-H bond length remains elongated (0.78 \AA). This is also reflected in the PDOS of $4\text{H}_2+\text{Ca@Gr}$ shown in Fig. 6(c), where the Ca $3d_{xy}$ and $3d_{x^2-y^2}$ states at the valence band edge overlap with H_2 $1\sigma^*$ state under zero field and -0.2 V \AA^{-1} electric field, whereas under a positive electric field the $3d_{z^2}$ state of Ca is overlapping with H_2 $1\sigma^*$. In addition, it can be seen that the exchange splitting between the occupied spin-up $3d_{z^2}$ state and the corresponding unoccupied spin-down state is about 0.5 eV under a positive electric field which indicates single-electron occupancy of this state. Under zero or negative electric field, the exchange splitting is smaller ($\sim 0.2 \text{ eV}$) and we see that the corresponding spin-down state is partially occupied. In addition, it can be seen from Fig. 6 that occupation of Ca states near the Fermi energy increases with the electric field decreasing (i.e., from $+0.2$ to -0.2 V \AA^{-1}). This corroborates that there is a higher density of electrons around the Ca adatom under zero and negative electric fields, facilitating a stronger Kubas interaction with H_2 molecules. By relaxing a single gas phase hydrogen molecule and the Ca@Gr substrate at -0.2 and 0.2 V \AA^{-1} electric force fields (along the same z direction), we find that the adsorption energy of 4H_2 on Ca@Gr is -211 and -167 meV , respectively, per H_2 molecule. The difference of $\sim 50 \text{ meV}$ in H_2 adsorption energy on Ca@Gr when applying -0.2 and 0.2 V \AA^{-1} electric force fields is consistent with the difference in the interaction energy reported in Fig. 5.

VII. CONCLUSION

We predicted H_2 adsorption energies and structures on alkali and alkaline-earth metal decorated graphene materials to understand how these substrates can facilitate H_2 adsorption. We find three distinct adsorption mechanisms which manifest from the electronic structure of the metal adatom. First, alkali metal adatoms act as positive charges interacting with H_2 molecules via attractive electrostatic interactions. Under this mechanism, the H_2 molecules are upright on graphene,

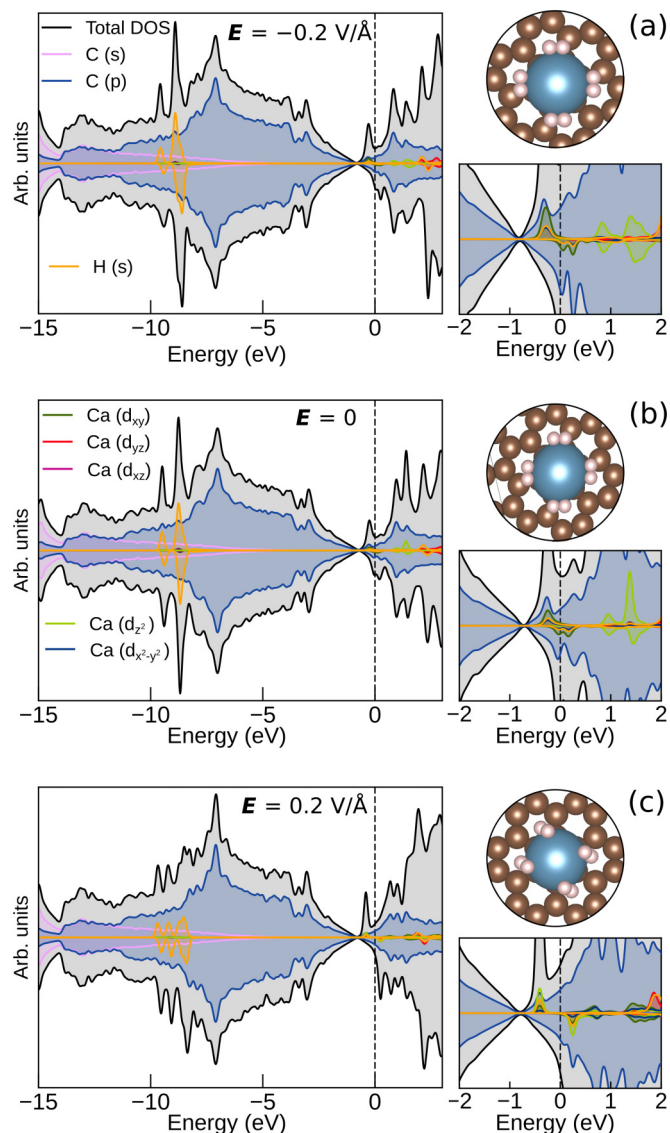


FIG. 6. Projected density of states (PDOS) for $4\text{H}_2+\text{Ca@Gr}$ with external electric fields of -0.2 V \AA^{-1} [(a), (b)], no field [(c), (d)], and $+0.2 \text{ V \AA}^{-1}$ [(e), (f)]. The left panel shows close-ups around the Fermi level (shifted to zero) of the corresponding PDOS on the right. The legend corresponds to all plots. The total DOS (black line, area shaded in gray) is normalized while the projected states are shown only if their contribution is more than 1%. The blue shaded regions correspond to C- p states. The projections over spheres centered on the atoms in the unit cell may not add up to the total DOS due to missing interstitial regions. The fully optimized adsorption structure at each electric field is also shown.

exposing the most electron-rich bonding region of the H_2 molecules to the positively charged adatom. Li@Gr best facilitates this mechanism of binding, with an adsorption energy of -187 meV per H_2 molecule in $3\text{H}_2+\text{Li@Gr}$. Second, small alkaline-earth metal atoms, Be and Mg, retain their gas phase electronic structure when adsorbed on graphene and have a negligible impact on adsorbing H_2 molecules, leading to weak physisorption. Larger alkaline-earth metals, i.e., Ca, Sr, and Ba, are partially depleted of valence electron density and more importantly, the d_{xy} and $d_{x^2-y^2}$ states of these atoms are stabi-

lized in favor of the gas phase valence s state. Therefore, in the third mechanism, H_2 molecules prefer to bind to the adatoms via Kubas bonding, receiving electron density into the H_2 $1\sigma^*$ state. This H_2 adsorption mechanism is distinguishable due to the resulting elongated H-H bond length. Kubas bonding also results in the strongest adsorption of H_2 among the materials we considered, with $4H_2$ molecules on Ca decorated graphene adsorbing at -190 meV per H_2 molecule. This is close to the adsorption strength we estimate to be necessary for viable H_2 storage (-200 to -400 meV) after approximating for zero-point energy vibrations and temperature effects. We derived this estimate of the H_2 adsorption energy window with ideal operating conditions in mind and a few approximations. Future works can increase the quantitative reliability in our work by applying more refined approximations for zero-point vibrations and temperature, and by establishing the accuracy of the DFT approximation. As part of this work, we also briefly considered the effects of a few physical features on H_2 physisorption—specifically, adatom diffusion, H_2 dissociation, and alternative substrates for graphene. In addition, we applied a range of external electric fields to a subset of systems and we find that the adsorption energy of H_2 is easily perturbed when H_2 molecules are bound via the Kubas interaction. Therefore, it is feasible that a metal decorated graphene system can be made into a viable storage material for hydrogen fuel. More generally, we expect the mechanisms outlined in this work to apply in similar adatom decorated materials. For example, covalent organic frameworks and metal organic frameworks are also promising low-dimensional storage materials, where alkali and alkaline-earth metals may play a similar role in binding H_2 . The experimental synthesis and clear characterization of such materials will be a key step toward the fruition of H_2 storage in low-dimensional materials. To this end, our results provide some useful indications of which materials to target and what properties can be probed, e.g., elongated H–H bonds. In summary, the findings provide a systematic overview of H_2 adsorption on alkali and alkaline-earth metal decorated graphene and form a basis for developing H_2 physisorption storage materials.

ACKNOWLEDGMENTS

Y.S.A. is supported by Leverhulme Grant No. RPG-2020-038. A.Z. also acknowledges support by Grant No. RPG-2020-038. The authors acknowledge the use of the UCL Kathleen High Performance Computing Facility (Kathleen@UCL), and associated support services, in the completion of this work. This research used resources of the Oak Ridge Leadership Computing Facility at the Oak Ridge National Laboratory, which is supported by the Office of Science of the U.S. Department of Energy under Contract No. DE-AC05-00OR22725. A.Z. acknowledges allocation of CPU hours by CSCS under Project ID s1112. This work has been performed using resources provided by the Cambridge Tier-2 system operated by the University of Cambridge Research Computing Service [61] funded by EPSRC Tier-2 capital grant (EP/T022159/1 and EP/P020259/1), and DiRAC funding from the Science and Technology Facilities Council [62]. This work also used the ARCHER UK National Super-

computing Service [63], the United Kingdom Car Parrinello (UKCP) consortium (EP/P022561/1).

APPENDIX: DERIVATION OF EQ. (1)

The H_2 vapor pressure is a key factor in determining the suitability of H_2 storage materials. Theoretical estimations of ideal H_2 vapor pressures have been proposed previously [64,65], resulting in about -150 to -600 meV adsorption energy range which is typically considered. The window of adsorption energies ultimately depends on several factors including the choice of fuel cells, device functionality, and the properties of the storage material. In our estimate we considered pressures from 3 bars to 100 bars and temperatures from 270 K to 390 K which covers intermediate and high temperature fuel cells [3,4]. In the following heuristic approach, we show how we evaluate the H_2 vapor pressure, using coronene as a model substrate for flat carbon based materials such as graphene, to arrive at our ideal adsorption energy estimate. We begin with the Gibbs free energy: $G(p, T) = U + pV - TS$, where p is pressure, T is temperature, U is the internal energy, V is volume, and S is entropy. The chemical potential, μ , is the Gibbs free energy normalized for the number of particles N : $\mu(p, T) = \frac{G(p, T)}{N}$. For the system at equilibrium, $\mu_{H_2@Gr} = \mu_{H_2} + \mu_{Gr}$, and we can separate the electronic contribution to the energy, E_{el} , which we compute from DFT, leaving the chemical potential of the phase state (ps), μ^{ps} : $\mu = E^{el} + \mu^{ps}$, where E^{el} accounts for the electronic energy at 0 K without zero-point energy contributions. According to Eq. (2), E_{ads} follows from the electronic contributions and thus we can write

$$0 = E_{ads} + \mu_{H_2@Gr}^{solid} - \mu_{H_2}^{gas} - \mu_{Gr}^{solid}, \quad (A1)$$

where the phase state is gas for H_2 and we assume $H_2@Gr$ and Gr are solids. As H_2 is a homonuclear diatomic gas we assume it here to be ideal such that $\mu_{H_2}^{gas}$ can be expressed as

$$\mu_{H_2}^{gas} = -k_B T \ln \frac{k_B T}{p \Lambda^3} - k_B T (\ln Z_r + \ln Z_v), \quad (A2)$$

where $\Lambda = \sqrt{\frac{h^2}{2\pi m_{H_2} k_B T}}$ is the de Broglie thermal wavelength, Z_r is the rotational partition function, and Z_v is the vibrational partition function. As a first approximation $Z_r \sim \frac{Ik_B T}{h^2}$,

where $I = \frac{m_{H_2} d_{H_2}^2}{4}$ is the moment of inertia. Within the harmonic approximation, the vibrational partition function is $Z_v = \frac{\exp(-\frac{\hbar\omega_{H_2}}{2k_B T})}{1 - \exp(-\frac{\hbar\omega_{H_2}}{k_B T})}$, where ω_{H_2} is the harmonic vibrational frequency of H_2 .

In the case of solids only phonons need to be considered (in the leading approximation, as the volumes are negligible with respect to the gas phase, so the pV term can be neglected), such that

$$\mu^{solid} = -k_B T \ln Z_v^{solid} \quad (A3)$$

for $H_2@Gr$ and Gr, where the vibrational partition function can be evaluated within the harmonic approximation as

$Z_v^{solid} = \prod_j \frac{\exp(-\frac{\hbar\omega_j}{2k_B T})}{1 - \exp(-\frac{\hbar\omega_j}{k_B T})}$; here ω_j is the vibrational frequency of the j th normal mode. $H_2@Gr$ has 6 more vibrational modes

than Gr due to 5 vibrations from H₂ interacting with Gr and 1 mode corresponding to the H₂ internal vibration. As a leading order approximation, we assume that the vibrations of H₂ and Gr are the same in H₂@Gr, which allows us to simplify $\mu_{\text{H}_2@\text{Gr}}^{\text{solid}} - \mu_{\text{Gr}}^{\text{solid}}$ in Eq. (A1) as follows:

$$\mu_{\text{H}_2@\text{Gr}}^{\text{solid}} - \mu_{\text{Gr}}^{\text{solid}} + k_B T \ln Z_{\nu}^{\text{H}_2} = -k_B T \ln Z_{i\nu}. \quad (\text{A4})$$

Here, $Z_{i\nu} = \prod_{j=1}^5 \frac{\exp(-\frac{\hbar\omega_j}{2k_B T})}{1 - \exp(-\frac{\hbar\omega_j}{k_B T})}$ is the vibrational partition function for the 5 intersystem modes, having the vibrational frequencies ω_j , $j = 1, \dots, 5$.

Thus, by using Eq. (A2) and Eq. (A4) in Eq. (A1), we arrive at an expression

$$-k_B T \ln \frac{k_B T}{p \Lambda^3} - k_B T \ln Z_r = E_{\text{ads}} - k_B T \ln Z_{i\nu}. \quad (\text{A5})$$

From this expression we extract the H₂ vapor pressure:

$$p = e^{\frac{E_{\text{ads}}}{k_B T}} \frac{k_B T}{\Lambda^3} \frac{Z_r}{Z_{i\nu}}. \quad (\text{A6})$$

In computing the vapor pressure, we can make a further approximation by assuming that physisorbed H₂ rotates freely such that Z_r drops out along with two intersystem vibrational frequencies (which are essentially H₂ rotating on the substrate). Furthermore, we assume that 2 intersystem vibrations parallel to the surface (xy plane) that are $\sim 80 \text{ cm}^{-1}$ are too weak for the harmonic approximation to be useful and thus we can neglect them, leaving us with the working equation

$$p \sim \frac{k_B T}{\Lambda^3} e^{\frac{E_{\text{ads}}}{k_B T}} \frac{1}{Z_{\nu_z}}. \quad (\text{A7})$$

Expanding Λ and Z_{ν_z} in Eq. (A7) yields Eq. (1). We consider the effect of this last approximation in Fig. 7 by comparison with using three intersystem vibrations (i.e., including those along the xy plane that we deem too weak for the harmonic approximation). We can see that the inclusion of the weak

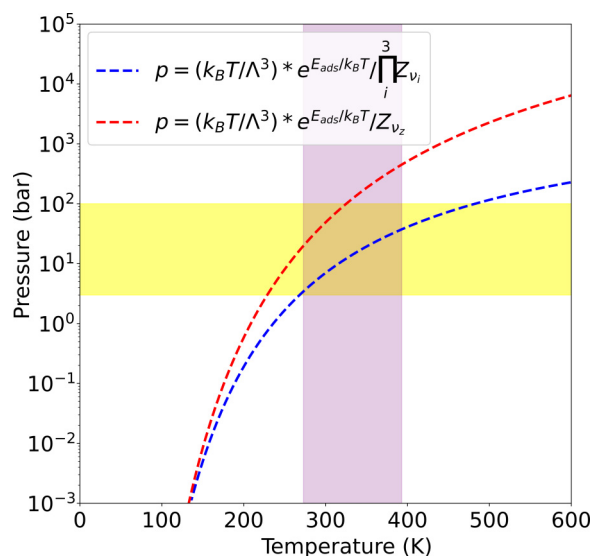


FIG. 7. Temperature-pressure adsorption profile for H₂ according to the approximations shown in the legend. The red line corresponds to Eq. (A7). An adsorption energy of -200 meV is used to demonstrate the effect of different approximations and PBE+D3 intersystem vibrational frequencies of the H₂-coronene molecular system.

vibrational modes would suggest that even lower adsorption energies could be sufficient at the operating conditions of a fuel cell.

Finally, it is important to note that we used a molecular system, H₂ on coronene, as a model for H₂ on pristine graphene, to have an estimate frequency ω_z , which is about 200 cm^{-1} . The ORCA quantum chemistry package [66] and the PBE+D3 functional were used to compute vibrational frequencies. For a more accurate pressure-temperature profile, the intersystem vibrational frequencies would need to be known for each substrate material that is considered. Nonetheless, it is interesting that our estimated window of ideal adsorption energy is consistent with previous estimations [64,65].

-
- [1] M. D. Allendorf, Z. Hulvey, T. Gennett, A. Ahmed, T. Autrey, J. Camp, E. Seon Cho, H. Furukawa, M. Haranczyk, M. Head-Gordon, S. Jeong, A. Karkamkar, D.-J. Liu, J. R. Long, K. R. Meihaus, I. H. Nayyar, R. Nazarov, D. J. Siegel, V. Stavila, J. J. Urban, S. P. Veccham, and B. C. Wood, An assessment of strategies for the development of solid-state adsorbents for vehicular hydrogen storage, *Energy Environ. Sci.* **11**, 2784 (2018).
- [2] N. Armaroli and V. Balzani, The hydrogen issue, *ChemSusChem* **4**, 21 (2011).
- [3] E. Ogungbemi, T. Wilberforce, O. Ijaodola, J. Thompson, and A. G. Olabi, Review of operating condition, design parameters and material properties for proton exchange membrane fuel cells, *Int. J. Energy Res.* **45**, 1227 (2021).
- [4] M. A. Salam, M. S. Habib, P. Arefin, K. Ahmed, M. S. Uddin, T. Hossain, and N. Papri, Effect of temperature on the performance factors and durability of proton exchange membrane of hydrogen fuel cell: A narrative review, *Mat. Sci. Res. India* **17**, 179 (2020).
- [5] A. Ahmed, S. Seth, J. Purewal, A. G. Wong-Foy, M. Veenstra, A. J. Matzger, and D. J. Siegel, Exceptional hydrogen storage achieved by screening nearly half a million metal-organic frameworks, *Nat. Commun.* **10**, 1568 (2019).
- [6] Y. S. Al-Hamdani, D. Alfè, and A. Michaelides, How strongly do hydrogen and water molecules stick to carbon nanomaterials? *J. Chem. Phys.* **146**, 094701 (2017).
- [7] Q. Lai, Y. Sun, T. Wang, P. Modi, C. Cazorla, U. B. Demirci, J. R. Ares Fernandez, F. Leardini, and K. Aguey-Zinsou, How to design hydrogen storage materials? Fundamentals, synthesis, and storage tanks, *Adv. Sustain. Syst.* **3**, 1900043 (2019).
- [8] K. Spyrou, D. Gournis, and P. Rudolf, Hydrogen storage in graphene-based materials: Efforts towards enhanced hydro-

- gen absorption, *ECS J. Solid State Sci. Technol.* **2**, M3160 (2013).
- [9] J. Wong, S. Yadav, J. Tam, and C. Veer Singh, A van der Waals density functional theory comparison of metal decorated graphene systems for hydrogen adsorption, *J. Appl. Phys.* **115**, 224301 (2014).
- [10] P. Reunchan and S. H. Jhi, Metal-dispersed porous graphene for hydrogen storage, *Appl. Phys. Lett.* **98**, 093103 (2011).
- [11] Y. Wen, F. Xie, X. Liu, X. Liu, R. Chen, K. Cho, and B. Shan, Tunable H₂ binding on alkaline and alkaline earth metals decorated graphene substrates from first-principles calculations, *Int. J. Hydrog. Energy* **42**, 10064 (2017).
- [12] Z. Amaniseyed and Z. Tavangar, Hydrogen storage on uncharged and positively charged Mg-decorated graphene, *Int. J. Hydrog. Energy* **44**, 3803 (2019).
- [13] Y. Y. Sun, K. Lee, L. Wang, Y.-H. Kim, W. Chen, Z. Chen, and S. B. Zhang, Accuracy of density functional theory methods for weakly bonded systems: The case of dihydrogen binding on metal centers, *Phys. Rev. B* **82**, 073401 (2010).
- [14] E. Beheshti, A. Nojeh, and P. Servati, A first-principles study of calcium-decorated, boron-doped graphene for high capacity hydrogen storage, *Carbon* **49**, 1561 (2011).
- [15] C. Ataca, E. Aktürk, and S. Ciraci, Hydrogen storage of calcium atoms adsorbed on graphene: First-principles plane wave calculations, *Phys. Rev. B* **79**, 041406 (2009).
- [16] W. Zhou, J. Zhou, J. Shen, C. Ouyang, and S. Shi, First-principles study of high-capacity hydrogen storage on graphene with Li atoms, *J. Phys. Chem. Solids* **73**, 245 (2012).
- [17] J. Cha, C. H. Choi, and N. Park, *Ab initio* study of Kubas-type dihydrogen fixation onto d-orbital states of Ca adatoms, *Chem. Phys. Lett.* **513**, 256 (2011).
- [18] S. Shepard and M. Smeu, First principles study of graphene on metals with the SCAN and SCAN+rVV10 functionals, *J. Chem. Phys.* **150**, 154702 (2019).
- [19] G. J. Kubas, Metal-dihydrogen and σ -bond coordination: The consummate extension of the Dewar-Chatt-Duncanson model for metal-olefin π bonding, *J. Organomet. Chem.* **635**, 37 (2001).
- [20] J. Cha, S. Lim, C. H. Choi, M. H. Cha, and N. Park, Inaccuracy of Density Functional Theory Calculations for Dihydrogen Binding Energetics onto Ca Cation Centers, *Phys. Rev. Lett.* **103**, 216102 (2009).
- [21] M. Bajdich, F. A. Reboredo, and P. R. C. Kent, Quantum Monte Carlo calculations of dihydrogen binding energetics on Ca cations: An assessment of errors in density functionals for weakly bonded systems, *Phys. Rev. B* **82**, 081405(R) (2010).
- [22] N. Park, K. Choi, J. Hwang, D. W. Kim, D. O. Kim, and J. Ihm, Progress on first-principles-based materials design for hydrogen storage, *Proc. Natl. Acad. Sci. USA* **109**, 19893 (2012).
- [23] W. Purwanto, H. Krakauer, Y. Virgus, and S. Zhang, Assessing weak hydrogen binding on Ca⁺ centers: An accurate many-body study with large basis sets, *J. Chem. Phys.* **135**, 164105 (2011).
- [24] Y. Ohk, Y.-H. Kim, and Y. Jung, Comment on “Inaccuracy of Density Functional Theory Calculations for Dihydrogen Binding Energetics onto Ca Cation Centers”, *Phys. Rev. Lett.* **104**, 179601 (2010).
- [25] T. D. Kühne, M. Iannuzzi, M. Del Ben, V. V. Rybkin, P. Seewald, F. Stein, T. Laino, R. Z. Khaliullin, O. Schütt, F. Schiffmann, D. Golze, J. Wilhelm, S. Chulkov, M. H. Bani-Hashemian, V. Weber, U. Borštnik, M. Taillefumier, A. S. Jakobovits, A. Lazzaro, H. Pabst, T. Müller, R. Schade, M. Guidon, S. Andermatt, N. Holmberg, G. K. Schenter, A. Hehn, A. Bussy, F. Belleflamme, G. Tabacchi, A. Glöß, M. Lass, I. Bethune, C. J. Mundy, C. Plessl, M. Watkins, J. VandeVondele, M. Krack, and J. Hutter, CP2K: An electronic structure and molecular dynamics software package - Quickstep: Efficient and accurate electronic structure calculations, *J. Chem. Phys.* **152**, 194103 (2020).
- [26] J. VandeVondele, M. Krack, F. Mohamed, M. Parrinello, T. Chassaing, and J. Hutter, Quickstep: Fast and accurate density functional calculations using a mixed Gaussian and plane waves approach, *Comput. Phys. Commun.* **167**, 103 (2005).
- [27] S. Goedecker, M. Teter, and J. Hutter, Separable dual-space Gaussian pseudopotentials, *Phys. Rev. B* **54**, 1703 (1996).
- [28] M. Krack, Pseudopotentials for H to Kr optimized for gradient-corrected exchange-correlation functionals, *Theor. Chem. Acc.* **114**, 145 (2005).
- [29] J. VandeVondele and J. Hutter, Gaussian basis sets for accurate calculations on molecular systems in gas and condensed phases, *J. Chem. Phys.* **127**, 114105 (2007).
- [30] See Supplemental Material at <http://link.aps.org/supplemental/10.1103/PhysRevMaterials.7.035402> for additional details on calculations and example input files.
- [31] J. P. Perdew, K. Burke, and M. Ernzerhof, Generalized Gradient Approximation Made Simple, *Phys. Rev. Lett.* **77**, 3865 (1996).
- [32] S. Grimme, J. Antony, S. Ehrlich, and H. Krieg, A consistent and accurate *ab initio* parametrization of density functional dispersion correction (DFT-D) for the 94 elements H-Pu, *J. Chem. Phys.* **132**, 154104 (2010).
- [33] T. Bučko, J. Hafner, S. Lebègue, and J. G. Ángyán, Improved description of the structure of molecular and layered crystals: *Ab initio* DFT calculations with van der Waals corrections, *J. Phys. Chem. A* **114**, 11814 (2010).
- [34] D. J. Carter and A. L. Rohl, Benchmarking calculated lattice parameters and energies of molecular crystals using van der Waals density functionals, *J. Chem. Theory Comput.* **10**, 3423 (2014).
- [35] P. O. Bedolla, G. Feldbauer, M. Wolloch, S. J. Eder, N. Dörr, P. Mohn, J. Redinger, and A. Vernes, Effects of van der Waals interactions in the adsorption of isooctane and ethanol on Fe(100) surfaces, *J. Phys. Chem. C* **118**, 17608 (2014).
- [36] J. Klimeš and A. Michaelides, Perspective: Advances and challenges in treating van der Waals dispersion forces in density functional theory, *J. Chem. Phys.* **137**, 120901 (2012).
- [37] J. Carrasco, J. Klimeš, and A. Michaelides, The role of van der Waals forces in water adsorption on metals, *J. Chem. Phys.* **138**, 024708 (2013).
- [38] M. Rosa, S. Corni, and R. D. Felice, Van der Waals effects at molecule-metal interfaces, *Phys. Rev. B* **90**, 125448 (2014).
- [39] E. Caldeweyher, C. Bannwarth, and S. Grimme, Extension of the D3 dispersion coefficient model, *J. Chem. Phys.* **147**, 034112 (2017).
- [40] A. Ambrosetti, A. M. Reilly, R. A. Distasio, and A. Tkatchenko, Long-range correlation energy calculated from coupled atomic response functions, *J. Chem. Phys.* **140**, 18A508 (2014).
- [41] A. Tkatchenko, R. A. Distasio, R. Car, and M. Scheffler, Accurate and Efficient Method for Many-Body van der Waals Interactions, *Phys. Rev. Lett.* **108**, 236402 (2012).

- [42] V. V. Gobre and A. Tkatchenko, Scaling laws for van der Waals interactions in nanostructured materials, *Nat. Commun.* **4**, 2341 (2013).
- [43] J. Neugebauer and M. Scheffler, Adsorbate-substrate and adsorbate-adsorbate interactions of Na and K adlayers on Al(111), *Phys. Rev. B* **46**, 16067 (1992).
- [44] G. Makov and M. C. Payne, Periodic boundary conditions in *ab initio* calculations, *Phys. Rev. B* **51**, 4014 (1995).
- [45] G. Kresse and J. Hafner, *Ab initio* molecular dynamics for liquid metals, *Phys. Rev. B* **47**, 558 (1993).
- [46] G. Kresse and J. Hafner, *Ab initio* molecular-dynamics simulation of the liquid-metal–amorphous-semiconductor transition in germanium, *Phys. Rev. B* **49**, 14251 (1994).
- [47] G. Kresse and J. Furthmüller, Efficient iterative schemes for *ab initio* total-energy calculations using a plane-wave basis set, *Phys. Rev. B* **54**, 11169 (1996).
- [48] G. Kresse and J. Furthmüller, Efficiency of *ab-initio* total energy calculations for metals and semiconductors using a plane-wave basis set, *Comput. Mater. Sci.* **6**, 15 (1996).
- [49] A. M. Ganose, A. J. Jackson, and D. O. Scanlon, sumo: Command-line tools for plotting and analysis of periodic *ab initio* calculations, *J. Open Source Softw.* **3**, 717 (2018).
- [50] G. Henkelman, A. Arnaldsson, and H. Jónsson, A fast and robust algorithm for Bader decomposition of charge density, *Comput. Mater. Sci.* **36**, 354 (2006).
- [51] G. Henkelman and H. Jónsson, Improved tangent estimate in the nudged elastic band method for finding minimum energy paths and saddle points, *J. Chem. Phys.* **113**, 9978 (2000).
- [52] G. Henkelman, B. P. Uberuaga, and H. Jónsson, A climbing image nudged elastic band method for finding saddle points and minimum energy paths, *J. Chem. Phys.* **113**, 9901 (2000).
- [53] D. Wong, F. Corsetti, Y. Wang, V. W. Brar, H.-Z. Tsai, Q. Wu, R. K. Kawakami, A. Zettl, A. A. Mostofi, J. Lischner, and M. F. Crommie, Spatially resolving density-dependent screening around a single charged atom in graphene, *Phys. Rev. B* **95**, 205419 (2017).
- [54] A. K. Singh and B. I. Yakobson, First principles calculations of H-storage in sorption materials, *J. Mater. Sci.* **47**, 7356 (2012).
- [55] W. Tang, E. Sanville, and G. Henkelman, A grid-based Bader analysis algorithm without lattice bias, *J. Phys.: Condens. Matter* **21**, 084204 (2009).
- [56] E. Sanville, S. D. Kenny, R. Smith, and G. Henkelman, Improved grid-based algorithm for Bader charge allocation, *J. Comput. Chem.* **28**, 899 (2007).
- [57] X. Liu, C. Z. Wang, M. Hupalo, W. C. Lu, M. C. Tringides, Y. X. Yao, and K. M. Ho, Metals on graphene: Correlation between adatom adsorption behavior and growth morphology, *Phys. Chem. Chem. Phys.* **14**, 9157 (2012).
- [58] C. Cazorla, S. A. Shevlin, and Z. X. Guo, First-principles study of the stability of calcium-decorated carbon nanostructures, *Phys. Rev. B* **82**, 155454 (2010).
- [59] F. Mittendorfer, A. Garhofer, J. Redinger, J. Klimeš, J. Harl, and G. Kresse, Graphene on Ni(111): Strong interaction and weak adsorption, *Phys. Rev. B* **84**, 201401(R) (2011).
- [60] F. Bianchini, L. L. Patera, M. Peressi, C. Africh, and G. Comelli, Atomic scale identification of coexisting graphene structures on Ni(111), *J. Phys. Chem. Lett.* **5**, 467 (2014).
- [61] See <https://www.hpc.cam.ac.uk>.
- [62] See <https://www.dirac.ac.uk>.
- [63] See <https://www.archer2.ac.uk>.
- [64] J. Li, T. Furuta, H. Goto, T. Ohashi, Y. Fujiwara, and S. Yip, Theoretical evaluation of hydrogen storage capacity in pure carbon nanostructures, *J. Chem. Phys.* **119**, 2376 (2003).
- [65] S. K. Bhatia and A. L. Myers, Optimum conditions for adsorptive storage, *Langmuir* **22**, 1688 (2006).
- [66] F. Neese, F. Wennmohs, U. Becker, and C. Riplinger, The ORCA quantum chemistry program package, *J. Chem. Phys.* **152**, 224108 (2020).